Structure of anthrax lethal toxin prepore complex suggests a pathway for efficient cell entry

Lucien Fabre,[1,2] Eugenio Santelli,[3] Driss Mountassif,[1,2] Annemarie Donoghue,[4,5,6] Aviroop Biswas,[1,2] Rikard Blunck,[4,5,6] Dorit Hanein,[3] Niels Volkmann,[3] Robert Liddington,[3]* and Isabelle Rouiller[1,2]*

[1]Department of Anatomy and Cell Biology and [2]Groupe de Recherche Axé sur la Structure des Protéines (GRASP), Groupe d'Étude des Protéines Membranaires (GÉPROM), McGill University, Montréal, Québec H3A 0C7, Canada
[3]Bioinformatics and Structural Biology Program, Sanford Burnham Prebys Medical Discovery Institute, La Jolla, CA 92037
[4]Departments of Physics, [5]Department of Physiology, and [6]Groupe d'Étude des Protéines Membranaires (GÉPROM), Université de Montréal, Montréal, Québec H3T 1J4, Canada

Anthrax toxin comprises three soluble proteins: protective antigen (PA), lethal factor (LF), and edema factor (EF). PA must be cleaved by host proteases before it oligomerizes and forms a prepore, to which LF and EF bind. After endocytosis of this tripartite complex, the prepore transforms into a narrow transmembrane pore that delivers unfolded LF and EF into the host cytosol. Here, we find that translocation of multiple 90-kD LF molecules is rapid and efficient. To probe the molecular basis of this translocation, we calculated a three-dimensional map of the fully loaded $(PA_{63})_7$–$(LF)_3$ prepore complex by cryo–electron microscopy (cryo-EM). The map shows three LFs bound in a similar way to one another, via their N-terminal domains, to the surface of the PA heptamer. The model also reveals contacts between the N- and C-terminal domains of adjacent LF molecules. We propose that this molecular arrangement plays an important role in the maintenance of translocation efficiency through the narrow PA pore.

The Journal of General Physiology

INTRODUCTION

Bacillus anthracis, the causative agent of anthrax, secretes three soluble proteins collectively known as "anthrax toxin." This tripartite toxin is composed of the receptor-binding subunit, the 83-kD protective antigen (PA_{83}), and the two toxic enzymatic subunits, the lethal and edema factors (LF and EF) with a molecular mass of ∼90 kD each (Friebe et al., 2016).

Anthrax toxin is actively involved during both the early and late steps of the infectious process. In the case of the most deadly form, inhalational anthrax (Plotkin et al., 2002), the classic "Trojan Horse" model of infection posits that spores engulfed by alveolar macrophages are transported past the lung epithelial barrier to lymph nodes. Germination and expression of exotoxins induces breaching of the phagosomal membrane (Banks et al., 2005), killing the macrophage from within and enabling bacilli to escape into the lymphatic system and enter vegetative outgrowth. An alternative, or complementary, "Jailbreak model" has been proposed, in which spores spontaneously germinate in the lungs and secrete anthrax toxins, enabling them to permeabilize tissue (Weiner and Glomski, 2012) and cross directly into the regional lymphatic system. Once at a regional lymph node, vegetative cells secrete toxins that incapacitate or kill immune cells, including macrophages, neutrophils, and activated monocytes, from without (Weiner and Glomski, 2012). This provides the time needed for massive outgrowth of vegetative spores, migration to the vasculature, and ultimately death via generalized destruction of the vascular and/or key organs (Liu et al., 2013).

To kill the cells of the host, the two enzymatic subunits LF and EF of the toxin need to gain access to the cell cytoplasm. They are transported there by the PA moiety. After binding to either one of its receptors, tumor endothelial marker 8 (TEM8) or capillary morphogenesis gene 2 (CMG2), at the cell surface, the 83-kD form of PA_{83} is cleaved by a furin-like protease and produces a shorter form, PA_{63} (Klimpel et al., 1992). PA_{63} then assembles into heptameric $(PA_{63})_7$ or octameric $(PA_{63})_8$ oligomers (Milne et al., 1994; Kintzer et al., 2009) that bind one to four copies of its "cargo" EF and LF and cluster in a lipid raft at the plasma membrane before being endocytosed (Abrami et al., 2003). Low endosomal pH triggers the conformational change from the prepore to the pore conformation (Miller et al., 1999). LF and EF are then translocated in an un-

*R. Liddington and I. Rouiller contributed equally to this paper.
Correspondence to Isabelle Rouiller: isabelle.rouiller@mcgill.ca; or Robert Liddington: rlidding@sbpdiscovery.org

Abbreviations used: CC, correlation coefficient; EF, edema factor; EM, electron microscopy; LF, lethal factor; PA, protective antigen; RMSD, root-mean-square deviation.

The Rockefeller University Press $30.00
J. Gen. Physiol. 2016 Vol. 148 No. 4 313–324
www.jgp.org/cgi/doi/10.1085/jgp.201611617

folded state (Thoren et al., 2009) to the host cell cytoplasm (Milne et al., 1995; Zheng et al., 2014) through a proton–protein symport mechanism (Krantz et al., 2005; Basilio et al., 2009; Wynia-Smith et al., 2012; Brown et al., 2015).

The structure of the prepore complex alone (Petosa et al., 1997), bound to its receptor (Lacy et al., 2004; Santelli et al., 2004), and bound to the N-terminal domains of LF (LF_N; Feld et al., 2010) have been solved by x-ray crystallography. The pore conformation has been solved by cryo–electron microscopy (cryo-EM; Katayama et al., 2010; Gogol et al., 2013; Jiang et al., 2015). In the pore conformation, the PA heptamer forms a membrane-spanning channel ∼180 Å long with a long β-barrel of 12–18-Å inner diameter, capped by a narrow constriction or iris of ∼6 Å, called the "Φ-clamp", which forms a watertight conduit for translocation of unfolded polypeptides, one at a time, through the lumen and into the cytosol. The translocation process is driven by (a) the nature of the pore, which is watertight and highly selective for positively charged and neutral residues; (b) the low pH of the late endosome, which promotes enzyme unfolding, attachment to the Φ-clamp, and neutralization of acidic residues; and (c) the pH gradient across the pore, which generates force via an "electrostatic Brownian ratchet" mechanism that drives unidirectional translocation. Although translocation in vitro does not require accessory factors, in the crowded environment of the cell, chaperones have been reported to facilitate enzyme unfolding and refolding (Tamayo et al., 2011; Slater et al., 2013).

Despite these impressive studies, important questions remain. Assembly of soluble components at the host membrane into an oligomeric toxin-laden complex that promotes receptor clustering and endocytosis must be carefully coordinated in time and space (Liu et al., 2014). How is this achieved? The prepore can hold a cargo of up to three (heptamer; Mogridge et al., 2002) or four (octamer; Feld et al., 2010) LF/EF molecules, which bind competitively via homologous 30-kD N-terminal domains (Pimental et al., 2004) to the upper rim of the prepore. The efficient translocation of multiple 90-kD toxic cargos from the denaturing environment of the late endosome to the cytosol through a single channel would seem to present a formidable challenge, although the efficiency of translocation is reported to be independent of the number of enzymes bound (Zhang et al., 2004). So how is decorum enforced? For example, does the prepore to pore transition influence binding? Is there a preferred order of translocation (and if so, which enzyme goes first)? And how do the enzymes "waiting in line" avoid premature unfolding that could interfere with translocation or promote dissociation from the pore?

To begin to address these questions, we first determined the structure of the PA heptamer fully laden with LF cargo using cryo-EM at a resolution of 16 Å and correlated these data with single-channel electrophysiological experiments that established the kinetics of LF translocation.

MATERIALS AND METHODS

Purification of $(PA_{63})_7$–$(LF)_3$

PA_{83} was expressed in *Escherichia coli* as a His-tagged protein and purified as previously described (Santelli et al., 2004). PA_{63} was generated by trypsin cleavage (nicking) of pure PA_{83} in vitro (1:2,500 molar ratio), and the nicked PA was loaded onto a monoQ ion exchange column (GE Healthcare) at pH 8.6 and eluted with a gradient of 0–0.6 M NaCl, which removes PA_{20} and leads to the spontaneous formation of $(PA_{63})_7$ prepores, which are water soluble at high pH. LF was purified as previously described (Park and Leppla, 2000). To confirm the binding stoichiometry of 7:3, $(PA_{63})_7$ prepores were incubated with increasing ratios of LF and run on a Superose 6 size exclusion/gel filtration column (GE Healthcare). For EM experiments, $(PA_{63})_7$ (500 µl at 230 nM) was incubated with a twofold excess of LF (25 µl at 10 µM), and the complex was separated on a Superose 6 column (Fig. 1 A). Peak fractions were collected, and the stoichiometry was confirmed by SDS-PAGE analysis and densitometry of Coomassie-stained bands (Fig. 1 B).

Electrophysiological recordings

For electrophysiological measurements, a horizontal bilayer system was used as described previously (Groulx et al., 2010). Over a 100-µm aperture in a polymer film, a planar lipid bilayer was formed from 25 mg/ml 1,2-diphytanoyl-sn-glycero-3-phosphocholine (DPhPC) in decane. The polymer film separated two chambers with the same buffer (10 mM ocalic acid, 10 mM MES, 10 mM phosphoric acid, 1 mM EDTA, and 250 mM potassium chloride) but different pH values; pH 5.6 for the upper (cis) chamber and pH 6.6 for the lower (trans) chamber. Chamber volumes were 0.07 ml and 3 ml for cis and trans, respectively. For single-channel recordings, 0.1 µl PA_{63} (0.023 µg/ml) was added to the upper chamber, and as soon as one conductive channel was observed, the upper chamber was carefully washed 10 times with 70 µl of buffer to remove excess PA_{63}. The potential difference was adjusted to −20 mV to block channel conductance, and full-length LF and LF_N were added to the upper chamber at different concentrations (0.09–0.18 µg/ml). Switching the potential difference to 80 mV enabled translocation of LF/LF_N, which effectively blocked ion conductance during translocation. Recordings were made using the Axopatch 200B amplifier (Axon Instruments) and GPatch software and analyzed using Analysis. GPatch and Analysis were both developed at the Department of Anesthesiology, Uni-

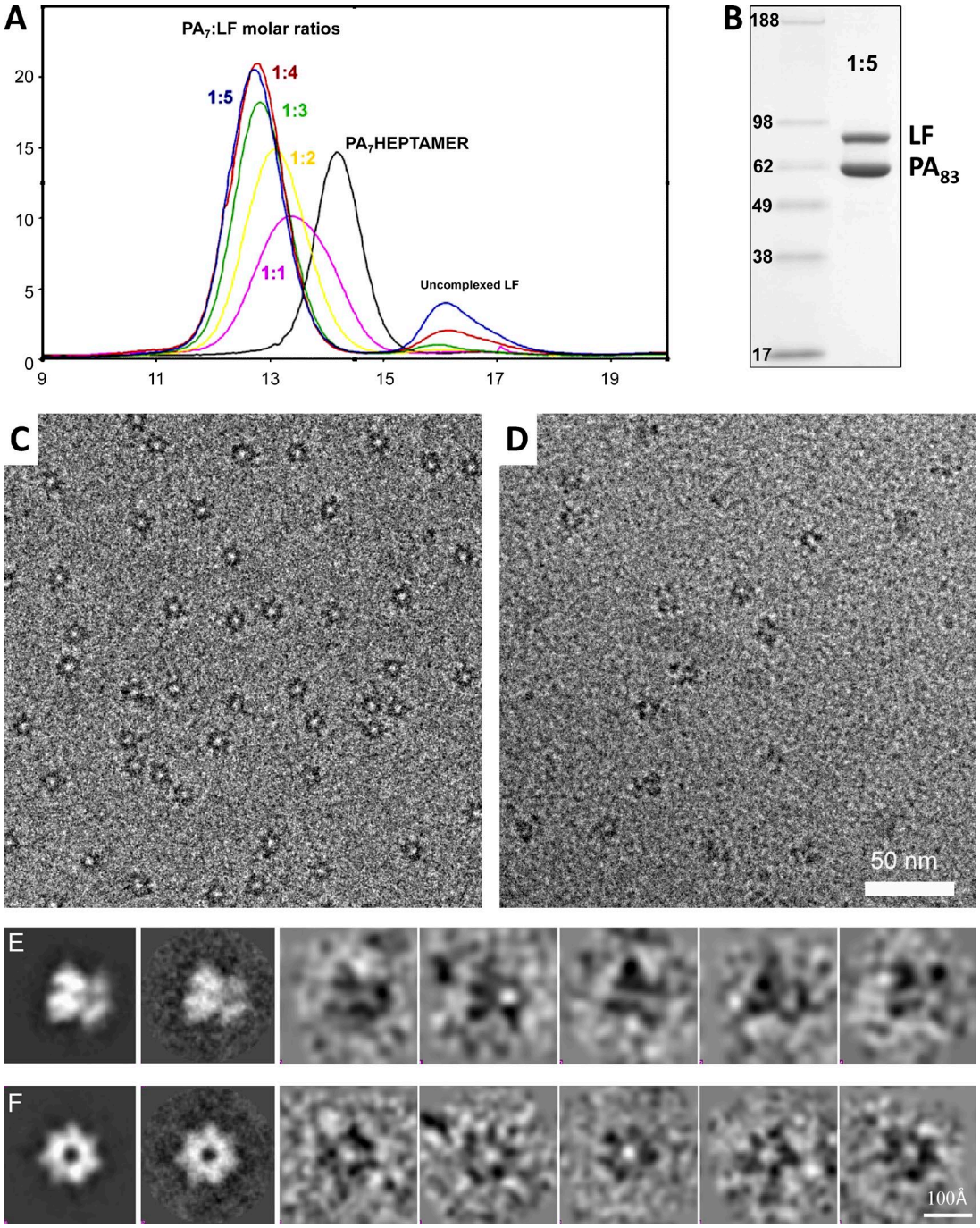

Figure 1. **Purification and imaging of the $(PA_{63})_7$–$(LF)_3$ complex.** (A) Superose 6 gel filtration shows a peak for the $(PA_{63})_7$ heptamer that shifts to higher mobility (larger size) when incubated with increasing ratios of LF. At a $(PA_{63})_7$/LF molar ratio of 1:3, saturation is somewhat <100% complete, owing to the low concentrations used. At 1:4 and 1:5 ratios, saturation is complete, and the major peak is consistent with a molecular ratio of 3:7 (LF/PA_{63}) (the peaks in the low molecular weight region comprise excess uncomplexed LF). (B) Coomassie-stained SDS-PAGE gel of purified $(PA_{63})_7$–$(LF)_3$ used for vitreous ice cryo-EM. Densitometry confirms a PA_{63}/LF ratio of 7:3. Molecular mass is indicated in kilodaltons. (C and D) Vitreous ice cryo-EM images of $(PA_{63})_7$–$(LF)_3$ complexes collected without (C) or with (D) pre-applying a layer of carbon to the EM grid in order to have the complexes adopting multiple orientations. (E and F) $(PA_{63})_7$–$(LF)_3$ complexes shown in two characteristic orientations, side view (E) and top view (F). The first column shows reprojection of the $(PA_{63})_7$–$(LF)_3$ reconstruction; second column, the corresponding 2-D class averages corresponding to the same orientation; third through seventh columns, examples of individual complexes $(PA_{63})_7$–$(LF)_3$ in the corresponding orientations. For viewing purposes, the contrast is inverted in the projections and averages; the raw images were low pass filtered to 40 Å.

versity of California, Los Angeles. Translocation times were determined from the duration of a single closing of the single pore in the presence of LF and LF_N (closed dwell time). Very short closings (<1 s) observed in the absence of LF/LF_N were excluded from analysis, as were very long closings (>100 s), which were not related to translocation either, as the pore reopened immediately upon reversal of the voltage to 20 mV.

EM sample preparation and data acquisition

Purified LF–PA_{63} complexes after gel filtration were diluted to 65 µg/ml in 1 mM $CaCl_2$, 150 mM NaCl, and 20 mM Tris-HCl, pH 8.0, and then applied to glow-discharged Quantifoil grids (Quantifoil Micro Tools GmbH) covered with a thin layer of carbon (Fig. 1, C–F). Grids were then blotted and frozen in liquid ethane slush. Frozen hydrated grids of LF–PA_{63} complexes were observed on a Tecnai F20 Twin transmission electron microscope (FEI Company) equipped with an FEG operated at 200 kV. Micrographs were recorded on ISO-163 plates (Eastman Kodak Co.) at a magnification of 50,000 with a total dose of 20–50$e^-/Å^2$ with defocus ranging from 1 and 5 µm. Micrographs were developed in full-strength Kodak D19 developer and digitized using a SCAI scanner (Integraph; Leica Geosystems) at 7 µm raster and binned to a final pixel size of 3.947 Å on the specimen.

Image processing and 3-D reconstruction

Particles were picked using the semiautomated routine Boxer of Eman (Ludtke et al., 1999). A total of 53,520 boxes were extracted from 96 micrographs. False positive were removed based on K-means 2-D classification with 32 classes using Sparx[v3] (Hohn et al., 2007), and 36,823 particles were retained (Fig. S1).

To generate the initial model, 11,061 particles were analyzed using the EMAN[1] package (Ludtke et al., 1999). Reconstructions were generated using seven different starting models (Fig. S2) refined with an angular sampling of 14.3° and low pass filtering at 30 Å at each iteration. Refinement was run until volumes became similar. These volumes were then aligned and merged using the align3d and avg3d commands of EMAN giving the starting model. Refinement of this initial model was conducted using XMIPP[v2.3] (Fourier reconstruction method; Scheres et al., 2008). Proper alignment of the gap was ensured by classification without realigning the particles (Fig. 2). The model obtained after classification was used for the final refinement.

After determining the contrast transfer function (CTF) using CTFIND3 (Mindell and Grigorieff, 2003), the final refinement was conducted with 36,823 particles using the Fourier reconstruction method of XMIPP[v2.3] with the following settings: 20 refinements for each the angular sampling rate (10°, 8°, 5°, 3°, 2°, and 1°) with respective angular search of 1,000 (unlimited), 20, 15, 9, 6, and 3. No limit was set for the maximum change in origin offset. The search range for 5-D translational search was set at five pixels for the first four iterations and one pixel afterward. Low pass filtering was performed at each iteration at the resolution estimated using the FSC criteria of 0.6 (0.5 + 0.1). The resolution of the final map was estimated to be at 16-Å resolution (Fig. 3 A). Analysis of our current dataset with other software did not improve resolution. The final map was corrected for envelope function and CTF amplitude effects using the model derived from fitting the x-ray structures (Volkmann and Hanein, 1999).

Fitting of known crystal structures into the reconstruction

Modular statistics–based rigid-body fitting (Volkmann and Hanein, 1999, 2003) of the PA prepore and LF crystal structures was used for quantitative characterization (Volkmann, 2009) of the reconstruction in light of the available high-resolution information. A rigid-body fitting approach was used as it is preferable over flexible fitting approaches at resolutions <10 Å because fewer free parameters need to be determined, leading to more robust results in terms of potential over-fitting (Volkmann, 2014). We used the 3-D watershed transform (Volkmann, 2002) to identify compact density compartments and their boundaries within the reconstructions in an unbiased fashion. The density of the reconstruction was then divided into segments corresponding to the PA portion and to each of the three LFs. The corresponding structures were iteratively fitted into the corresponding segments as previously described (Volkmann, 2009; Xu et al., 2012). Statistics were compiled, using a confidence level of 0.9995. The statistics indicate (a) there is no advantage in breaking up the PA or the LF into smaller domains, the resulting fits are statistically indistinguishable at 0.9995 confidence level from the fits using the complete PA and LF crystal structures; (b) there is no advantage in fitting the three LFs individually, the fit is statistically indistinguishable at 0.9995 confidence level from fitting with enforced symmetry; (c) all solutions compatible with the data fall into a narrow cluster with an average root-mean-square deviation (RMSD) of 2.48 Å ranging from 0.85 Å near the PA interface to 4.39 Å at the tip of the LF (around residue 712; Fig. 3 B), indicating some conformational breathing at that end. To test for statistical differences between the two alternative conformations of the LF_N α1–β1 segments with minimal bias from the rest of the structure, statistics were calculated using only slices of the experimental and calculated densities that contain a contribution of the segment in one or both of the two alternative conformations. The statistics indicate that the open conformation fits the experimental data significantly better than the alternative at a confidence level of 0.9995 for all three LF molecules.

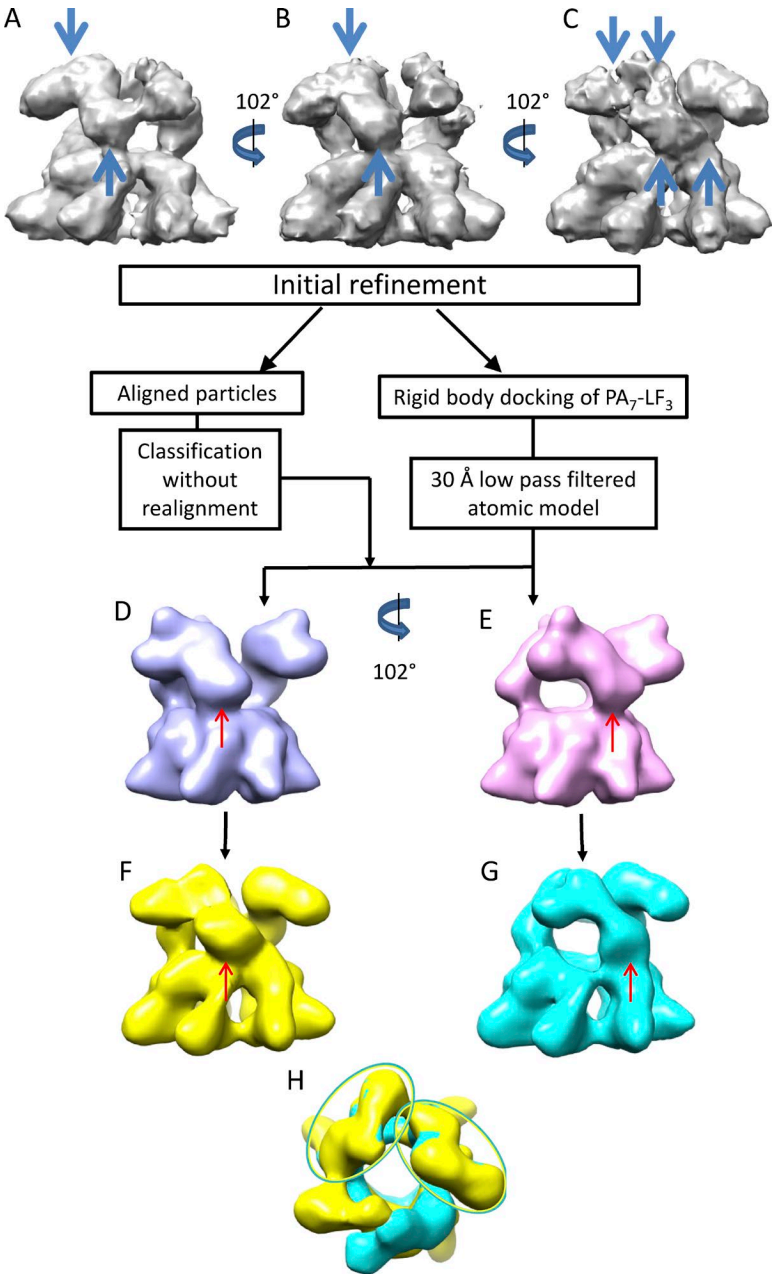

Figure 2. **Alignment of $(PA_{63})_7$–$(LF)_3$ complexes.** (A–C) The volume obtained after initial refinement is shown in three orientations. The densities corresponding to ^{1}LF (C) are double as highlighted with the arrows. An atomic model was generated by rigid-body docking of LF (1JKY; Pannifer et al., 2001) and $(PA_{63})_7$ (Lacy et al., 2004) into this volume and used as reference (D and E) after low pass filtering at 30 Å to ensure correct alignment of the large gap between ^{1}LF and ^{3}LF. Classification was performed without realigning the particles. The red arrows highlight the position of LF with respect to $(PA_{63})_7$. ~70% of the particles were found to be oriented as shown in F, whereas ~30% were oriented as in G. The orientations of volumes shown in F and G are compared with H in the top view orientation. The yellow and cyan ovals indicate overlapping densities corresponding to LF.

Modeling the $(PA_{63})_7$–$(LF)_3$ complex

A model of the complex was initially generated by rigid-body docking of the PA_{63} prepore (1TZO; Lacy et al., 2004) and three full-length LF molecules (PDB no. 1JKY; Pannifer et al., 2001) into the 16-Å EM map, followed by local energy refinement of the PA–LF interface using FireDock (http://bioinfo3d.cs.tau.ac.il/FireDock). The latter allows for small rigid-body movements and side-chain reorganization. This model agreed within experimental error with the locations of the LF_N domains in the octameric $(PA_{63})_8$–$(LF_N)_4$ complex (PDB no. 3KWV; Feld et al., 2010). We therefore made minor adjustments to the location of LF_N to match the crystal structure by overlaying the cognate PA_{63}–LF fragments via a least-squares fit on the PA_{63} moieties (RMSD = 1.9 Å). When the crystallographic model of full-length LF was overlaid onto the main body of LF_N (RMSD = 0.9 Å; i.e., excluding the N-terminal α1β1 helix-strand), the large 60-kD C-terminal fragment of LF fit perfectly into our map without any further adjustments necessary. Two models were generated, using the two alternative conformations of the α1β1 strand. Using the full-length LF crystal structure, we observed a steric clash between the α1β1 N-terminal region and a C-terminal segment of the counterclockwise neighbor (for both ^1LF_C–^2LF_N and ^2LF_C–^3LF_N). This steric clash disappeared using the open conformation of LF_N, but still left a significant contact region between LF_C–LF_N as observed in our maps. Furthermore, quantitative fitting gave a superior fit for the open LF_N

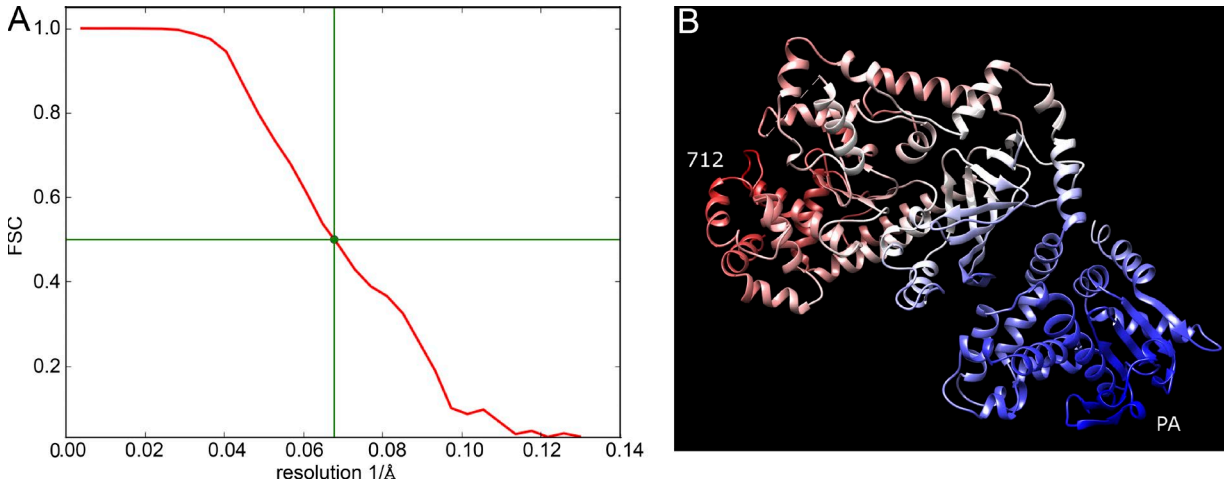

Figure 3. **Resolution of the EM map and accuracy of model building.** (A) Fourier shell correlation curve. According to the 0.5 forward scatter (FSC) criteria, the resolution of the final EM map is ~15 Å. (B) Accuracy of LF docking in the EM map. Blue corresponds to low RMSD (0.85 Å) and red to high RMSD (4.39 Å). The overall average RMSD is 2.48 Å.

conformation (Feld et al., 2010) into the density. The final model derived from the $(PA_{63})_7$–$(LF_N)_3$ map therefore comprised rigid body fitting of (a) the heptameric prepore; (b) a model for LF_N based on the rigid body of LF, and refined by reference to the octamer complex; and (c) the full-length LF from the isolated crystal structure, derived by overlay onto LF_N (with the exception of a small N-terminal segment [Feld et al., 2010]), which agreed within experimental error with the initial rigid-body fitting.

Online supplemental material

Fig. S1 shows raw data analyzed by 2-D classification. Fig. S2 shows initial model generation.

RESULTS

Cryo-EM structure of the fully loaded $(PA_{63})_7$–$(LF)_3$ complex

The only previously published structure of the PA–LF prepore complex in an EM reconstruction of a single LF molecule bound via its N- and C-terminal domains (LF_N and LF_C, respectively) to the PA heptamer, which had a partially broken ring (Ren et al., 2004; Tama et al., 2006). However, this structure could not be reconciled with the established stoichiometry of three LF/EF molecules bound per heptamer, the extensive biochemical mapping of the interaction surfaces between PA_{63} and LF_N (Cunningham et al., 2002; Lacy et al., 2002), or the crystal structure of the octameric prepore bound to four LF_N molecules (Feld et al., 2010). We therefore first sought a new and definitive model of the prepore, fully laden with three full-length LF enzymes.

We assembled such a complex in vitro by mixing preformed $(PA_{63})_7$ heptamers with LF, which produced a $(PA_{63})_7$–$(LF)_3$ complex with the expected stoichiometry (Cunningham et al., 2002; Mogridge et al., 2002), as judged by gel filtration and SDS page (Fig. 1). We then determined the structure of this complex at neutral pH in vitreous ice to 16-Å resolution using single-particle cryo-EM methods (Figs. 1, 2, and 3; and Figs. S1 and S2). Our map bears little resemblance to the previously published $(PA_{63})_7$–$(LF)_1$ structure. Instead, it displays a highly symmetric (sevenfold) core, with three large inverted L-shaped densities on top (Fig. 4). Initial rigid-body fitting of crystal structures of the $(PA_{63})_7$ prepore (Lacy et al., 2004) into the symmetric core and three full-length (monomeric) LF molecules (Pannifer et al., 2001) into the L-shaped densities gave excellent fits that accounted for most of the density (overall correlation coefficient [CC] = 0.94). The conformations of the three LF molecules and their interactions with PA protomers are nearly identical at this resolution (Fig. 4). We also note that no quaternary changes within LF (e.g., hinge bending between the LF_N and LF_C) were observed; indeed, the three densities were identical with a cross-correlation >0.98. Image analysis showed the absence of octamers in our assembly conditions.

All contacts between PA and LF involve the N-terminal domain of LF (LF_N) and the outer rim of the PA heptamer. There are no contacts between the 60-kD C-terminal domains of LF (LF_C) and PA. Instead, the three LF_C moieties wrap around the heptamer axis, but between 30 and 80 Å above the plane of the heptamer upper rim. We observed, however, substantial interactions between the LF_C moiety of one molecule and the LF_N moiety of its clockwise neighbors, forming a "daisy chain" of head to tail interactions (Fig. 4, B and C). Given that the footprint of each LF on the heptamer spans two adjacent PA_{63} protomers, the three bound LF molecules leave a single "orphan" PA_{63} between two LF molecules (~50 Å GAP; Fig. 4, C, E, and F). Thus, given

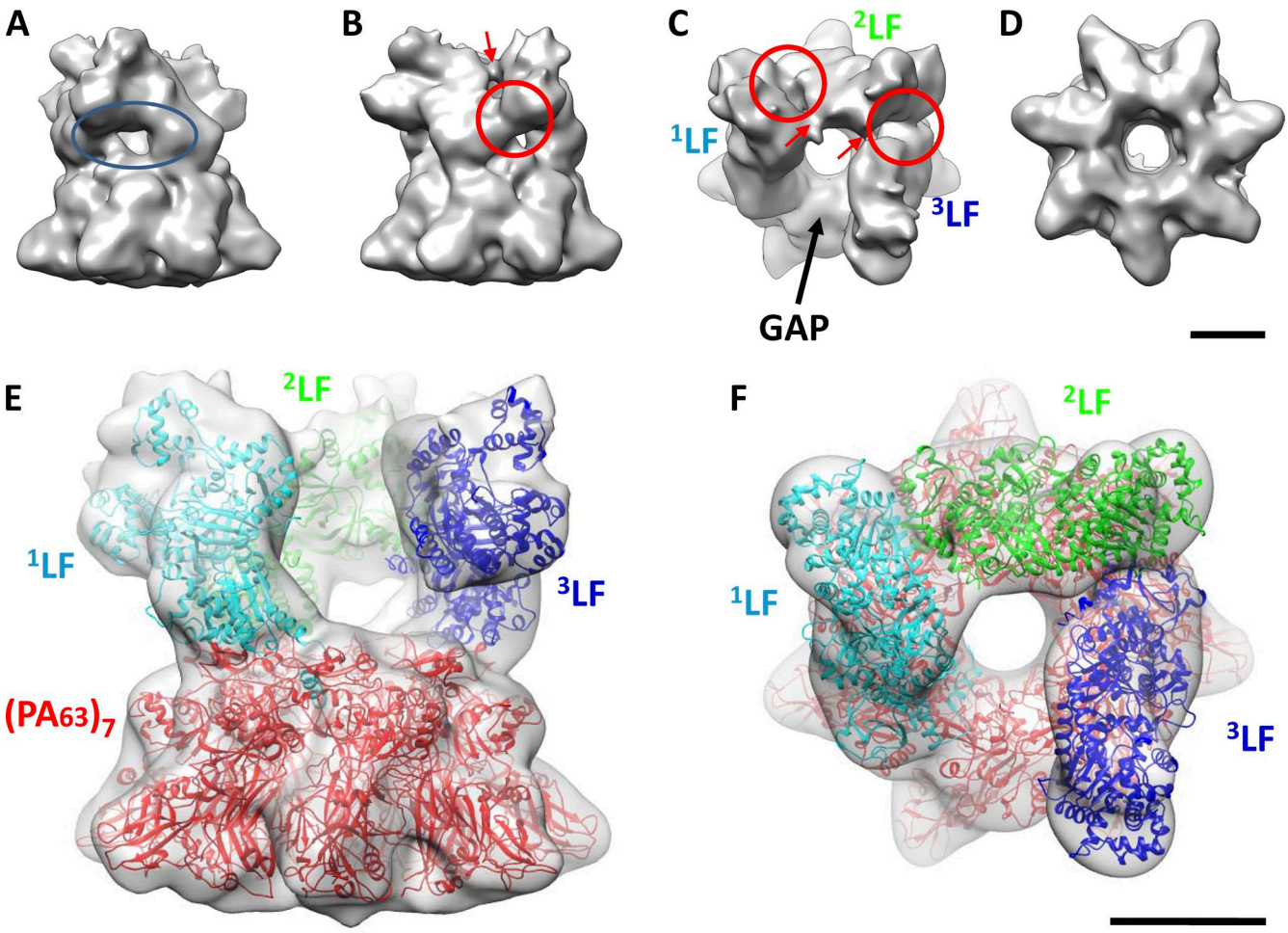

Figure 4. **3-D map of the $(PA_{63})_7$–$(LF)_3$ complex and its atomic interpretation.** (A–D) The map of $(PA_{63})_7$–$(LF)_3$ obtained by cryo-EM single-particle reconstruction at 16-Å resolution is shown in isosurface representation. (A) Side view showing the upside down L shape of LF molecules with a gap of ~30 Å tall (blue oval) between the surface of PA and the LF_C domains. (B) Side view, rotated about a vertical axis by ~100° counterclockwise compared with A, showing the major intermolecular LF_C–LF_N interaction within the complex (circled in red here and in C), and a minor contact visible at lower contour levels (red arrows here and in C). (C) Top-down view of the complex showing three LF molecules, each in unique environment (named from above ^{1}LF, ^{2}LF, and ^{3}LF; see F), Note the "gap" (marked by black arrow) caused by the symmetry mismatch, the major intermolecular LF_C–LF_N (circled in red), and the minor contact visible at a lower contour level (red arrows). (D) View from below reveals the strong sevenfold symmetry of $(PA_{63})_7$, which was not imposed during refinement. (E and F) Atomic models derived by rigid-body docking of component crystal structures into the EM map. The view in E looks directly into the gap, which overlooks the orphan PA_{63} moiety and is a rotation of A by 100° clockwise. The view in F is the same as C. The three LF molecules fit their respective densities with CC > 0.98, whereas the junctions between the LF molecules and their cognate PA molecule have CC > 0.97. Bars, 50 Å.

this mismatch of symmetries, each LF molecule has a unique environment. We define a clockwise (viewed from above) chain of linked molecules, ^{1}LF–^{2}LF–^{3}LF, in which ^1LF_C contacts ^2LF_N, and ^2LF_C makes similar contacts with ^3LF_N. However, ^1LF_N and ^3LF_C are adjacent to the orphan PA_{63} and do not interact with analogous LF partners. ^3LF_C is suspended above the heptamer, free from contacts with other molecules, and yet, as noted, it maintains the same quaternary conformation of the other two LF molecules.

Our rigid-body docking demonstrated that the packing between LF_N and PA_{63} is nearly identical to that observed in the crystal structure of LF_N bound to the octameric prepore (Feld et al., 2010). In the octamer complex (Feld et al., 2010), however, there is refolding of a short N-terminal α1–β1 segment (residues 29–51) of LF_N, compared with the solution structure of LF (Pannifer et al., 2001), in which the β1 strand peels away from the end of its sheet, enabling helix α1 to swing around and insert into a pocket on the inner rim of the prepore (this has been called the open conformation). We found that this open conformation fitted significantly better into our EM map than the closed conformation (confidence level of 0.9995) for all three LF molecules. We therefore rebuilt these residues to generate our final model as described in detail in Mate-

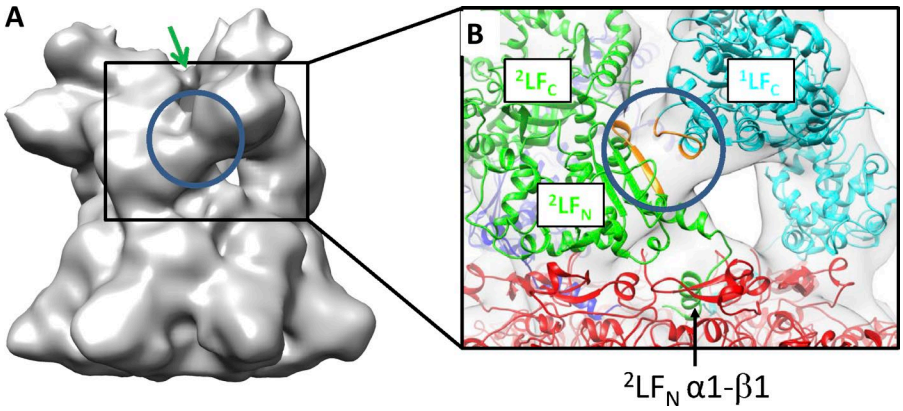

Figure 5. **LF head to tail interactions in $(PA_{63})_7$–$(LF)_3$.** (A) The C-terminal domain of LF (^1LF_C) establishes a large contact with the N-domain of the adjacent LF molecule (^2LF_N). This interaction (blue circle) is shown in the EM map displayed at two different contour levels (131,000 A^3 and 112,000 A^3 in A and B, respectively). Two adjacent LF_C domains establish a minor interaction (marked by a green arrow) that is broken at the higher threshold (see B). A very similar interaction is observed between ^2LF_C and ^3LF_N. (B) Close-up with two atomic models of LF fit into the density. The top of the PA_{63} heptamer (shown in red) is just visible. The blue circle highlights the novel ^1LF_C–^2LF_N interaction with coloration in orange of segments 572–579 of ^1LF_C and 75–83 of ^2LF_N. This region is identical in our model for ^2LF_C–^3LF_N. The black arrow highlights the position of the α1–β1 segment of ^2LF_N, which has been modeled in the open conformation (similar to the conformation solved by x-ray crystallography for $(PA_{63})_8$–$(LF_N)_4$ reported in Feld et al. [2010]) and is an identical position for ^1LF_N and ^3LF_N.

rials and methods. We note that this revised model eliminates steric clashes with LF_C predicted by our initial rigid-body model but does not eliminate contacts between LF_C (a C-terminal helix/loop, residues 573–583) and the N-terminal sheet of LF_N of its counterclockwise neighbor, as indicated by the strong intermolecular density noted above (Figs. 4 B and 5).

Efficient and rapid translocation of the full-length LF

We were intrigued by the LF_C–LF_N contacts and how they might affect translocation rates and efficiency. It has been reported that the efficiency of LF translocation is independent of the degree of LF loading onto the prepore (Zhang et al., 2004). However, quantitative measures of translocation times have only been reported for LF_N (Wynia-Smith et al., 2012). We therefore used an in vitro system to quantify and compare LF and LF_N translocation. In lipid bilayers, PA pores form ion-conductive (cation-selective) channels that are blocked when LF is translocating through the lumen and open again once translocation is complete. We conducted electrophysiological experiments in which a single PA_{63} heptamer was inserted into a synthetic lipid bilayer that separated cis and trans compartments buffered to pH values of 5.6 and 6.6, respectively. LF or LF_N in solution at nanomolar concentration was then introduced into the cis compartment, and translocation was controlled by manipulating the potential difference across the membrane. With a single channel, channel blockage time served as a simple surrogate for translocation time (Fig. 6). At this protein concentration range, translocation is not limited by the diffusion rate from bulk solution to the pore, and reopening of the pore could still be observed. Under these conditions, we found that full-length LF took three-times longer to translocate than LF_N (with a mean of 7.5 s vs. 2.5 s for LF vs. LF_N; Fig. 6, B–D). Given that the LF sequence is approximately three-times longer than LF_N, this suggests that both the N-terminal domain, LF_N, and the full-length LF molecule translocate at a similar rate (per residue) under these conditions.

At higher LF concentrations, although we still detected a prominent "fast" fraction (42% <9 s), we also observed longer pore blockage times (up to 1 min), which we interpret to be sequential and highly coordinated translocation of LF molecules, such that no detectable pore opening is observed in between molecules. We hypothesize that under these conditions, rapid, sequential recruitment of LF from solution to the heptamer generates a "fully loaded," fully operational, continuously translocating prepore. As one LF molecule is completing its translocation, the adjacent LF freed up from interactions starts to be translocated immediately, and the empty location is rapidly occupied by a new LF molecule from the solution phase. That is, the pore can remain effectively fully loaded for extended periods, acting as a conveyor belt while translocating a continuous daisy chain of LF molecules for long periods.

DISCUSSION

Our EM reconstruction map of the PA–LF prepore complex reveals three LF molecules bound to the $(PA_{63})_7$ prepore, with each LF molecule "standing up," perched atop the upper rim of the prepore via its small LF_N domain, and with its large C-terminal domain suspended high (up to 50 Å) above the rim. Our structure clearly demonstrates that two pairs of LF molecules make head to tail interactions between their C-terminal helix/loop (residues 573–583) and the N-terminal β sheet of their clockwise neighbor (a region that is critical for initiation of and rate limiting for translocation [Thoren et al., 2009]). We hypothesize that these ar-

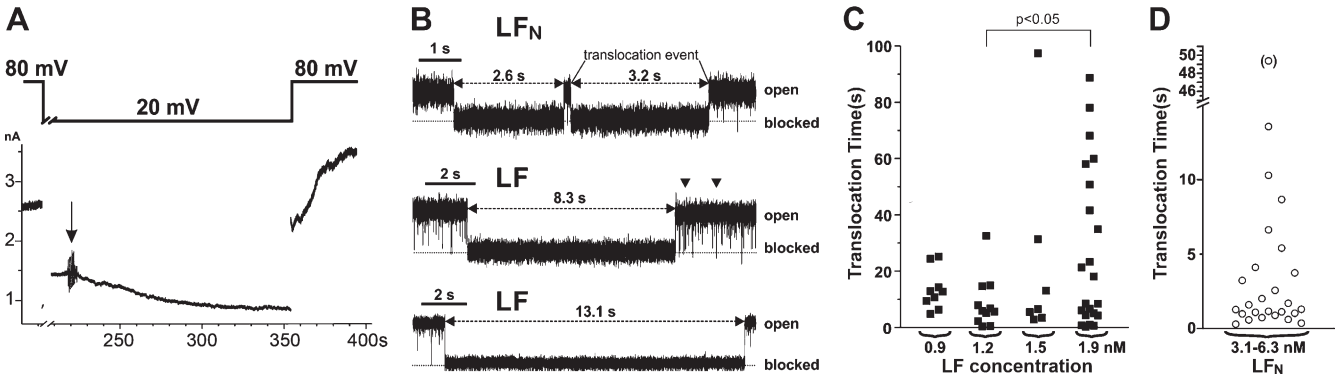

Figure 6. **Electrophysiological measurement of translocation of LF through a single pore.** A horizontal lipid bilayer system was used, which separates compartments with different pH values; pH 5.6 for the upper (cis) chamber and pH 6.6 for the lower (trans) chamber as described previously (Groulx et al., 2010; see Materials and methods). (A) Translocation of LF through PA_{63}. To test function of the proteins and verify translocation of LF through PA_{63}, PA_{63} was added to the cis chamber, and once a macroscopic current at 80 mV was observed, the voltage was switched to 20 mV and LF or LF_N was added (arrow). At 20 mV, LF will block the pore without being translocated. Blockage of the pore was evident by reduced current. Switching the membrane potential back to 80 mV enabled translocation of LF/LF_N through the pore, and once complete, the current increased again. (B) Translocation times for analysis were determined from single-channel recordings; example traces of single translocation events are shown for LF_N (top) and LF (middle and bottom). The dashed lines mark the translocation event, and the arrows indicate short (<1 s) spontaneous closings that were also observed in the absence of LF/LF_N and were thus ignored in the analysis. The dotted lines indicate the blocked PA. (C) The duration of single pore closings (translocations) at various concentrations of full-length LF is shown in a cloud plot. Each point represents a single measurement such as shown in B. Pore closure times at high concentrations were statistically different to the lower concentrations of LF ($P < 0.05$). (D) Pore closure times for LF_N showed no concentration dependence, and the data were pooled. Closure times for LF_N were statistically different from those of full-length LF ($P < 0.005$). Statistical significance was tested with one-way ANOVA.

rangements create both order and stability by holding the N termini in place and preventing further unfolding of the N-terminal domains. This elaborate architecture may also protect toxin complexes from unwanted attacks by proteases located at the cell surface or in the endocytic compartments. In the case of a fully loaded heptamer, the symmetry mismatch leads to the N-terminal domain of ^{1}LF to be uniquely unfettered by packing against other LF molecules. It seems therefore reasonable that ^{1}LF should translocate first. Once this is completed, ^{2}LF is then freed from its inhibitory bonds to ^1LF_C and may translocate next, followed finally by ^{3}LF. In addition, the inter-LF bonds may serve to inhibit premature unfolding/dislocation of the LF molecules waiting in line as the environment of the late endosomes becomes increasingly acidic. We note that with the N terminus of ^{2}LF in position, it may start a pseudo-continuous translocation process, rapidly following the C-terminal tail of ^{1}LF into the lumen, as we deduced from our electrophysiology experiments. Further studies are required to assess whether the interactions between LF_C and the adjacent LF_N are sufficient to dictate the order in which the LF molecules are translocated. We also showed that the density of LF is most consistent with the pro-translocation N-terminal reorganization seen in the octameric crystal structure. In that conformation, the unfolded N terminus of LF (residues 1–22, not solved by x ray) is thereby long enough to reach the pore Φ-clamp site without requiring unfolding of its LF_N domain. It therefore cannot be excluded that the order of translocation is dictated by which LF reaches the Φ clamp of the pore first in a stochastic manner.

Our electrophysiology experiments show that translocation occurs rapidly and efficiently even in the presence of a large excess of LF and that translocation occurs as rapidly for LF and LF_N in terms of translocation per residue. In vivo, the number of LF moieties per PA oligomer may vary with the time (early or late stages of infection) and the site of infection. Using a cell-based system, the efficiency of translocation of LF_N was demonstrated to be independent of the number of LF_N ligands (Zhang et al., 2004). It is unlikely that a large excess of free LF molecules, as used in our electrophysiology set-up, would arise in vivo. Nonetheless, our observations are consistent with a pore that acts as a robust, efficient translocation machine, one that continues to function under extreme conditions irrespective of the number of ligands.

We note that both the PA_{63} heptamer and LF do not undergo large conformational changes and remain close to the conformations observed in the isolated crystal structures (Petosa et al., 1997; Pannifer et al., 2001; Lacy et al., 2004; Santelli et al., 2004; Feld et al., 2010). That is, $(PA_{63})_7$ maintains its sevenfold symmetry, and the conformations of the three LF molecules are identical to one another in our map and nearly identical to that of the isolated LF molecule (Pannifer et al., 2001). Our map is quite distinct from the previously published cryo-EM reconstruction of $(PA_{63})_7$ bound to one full-length LF (Ren et al., 2004), where the single LF mole-

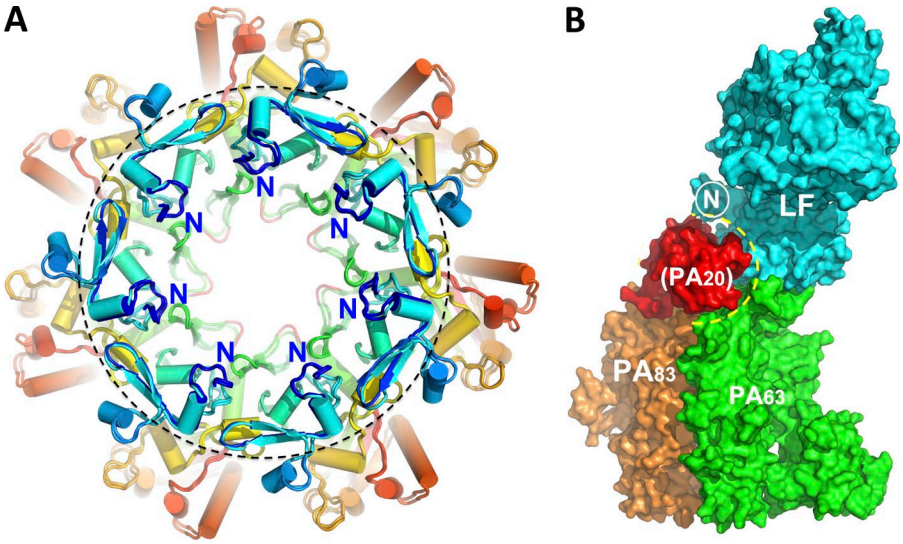

Figure 7. **Compatibility of our model with previous structures.** (A) Comparison of the prepore and pore rims. Domains 1a and 3 from the prepore (cyan/orange) and pore (blue/red) are overlaid. The RMSDon Cαs for the top of the rim (seven domains 1a, residues 176–250) and the rim (seven domains 1a and 3, residues 176–250 + residues 458–496) is 1.48 Å. The black ring denotes the outer limit of LF contacts, and the blue "N"s denoted the innermost contacts. (B) Hypothetical model of an assembly intermediate, a PA_{83}–PA_{63}–LF complex. Starting with a $(PA_{63})_2$–LF moiety extracted from our EM structure, the location of PA_{20} was predicted by overlaying the crystal structure of domain 1 of full-length PA_{83} onto domain 1a of the counterclockwise PA_{63} protomer, creating a new PA_{83} protomer (shown in orange and red; as described as in Material and methods section Modeling the $(PA_{63})_7$–$(LF)_3$ complex). No major steric clashes were observed between the new PA_{20} moiety and the clockwise PA_{63} protomer (green), which makes the major interactions with LF. However, only the closed conformer of LF is compatible with the presence of PA_{20}. The circled "N" marks the first ordered helix of closed LF, which is sterically occluded from reorganizing and entering the channel pore. The yellow dashed line indicates novel interfaces that could stabilize the intermediate.

cule lay on its side on top of $(PA_{63})_7$, interacting with four successive PA_{63} monomers, and partially closing the $(PA_{63})_7$ lumen. In that map, the sevenfold symmetry of $(PA_{63})_7$ was not maintained, and both LF and the interacting PA subunits underwent large conformational changes (Ren et al., 2004; Tama et al., 2006). A possible explanation for the observed differences may lie in the different methodological approaches. Specifically, we used a carbon substrate, whereas Ren et al. (2004) added β-octylglucoside. It has been reported that β-octylglucoside increases the pH below which the heptamer becomes SDS resistant (i.e., pore-like [Miller et al., 1999]). It is thereby possible that the previous reconstruction captured the complex at a different stage along the pathway of translocation. However, it is worth reiterating that our electrophysiology measurements demonstrate rapid and efficient translocation of full-length LF even at very high concentrations of LF. That is, our experiments support a model in which the pore remains intact during many translocation events, quite incompatible with a pathway in which the PA_{63} pore loses its structural integrity.

In our model, the binding footprint of LF_N, which spans two sequential PA_{63} protomers, is fully consistent with the binding mode observed in the octameric prepore bound to LF_N (Feld et al., 2010), as well as earlier models from Collier's group based on an elegant series of mutagenesis experiments (Cunningham et al., 2002; Lacy et al., 2002) and our modeling experiments (Alisaraie and Rouiller, 2016). The surface of PA_{63} that interacts with LF is preserved between the octamer and the heptamer. A comparison of the two adjacent PA_{63} subunits in the heptamer and octamer indicates an RMSDon Cαs of 1.07 Å (domains 1a and 3). Of particular note, the LF-binding surface on the $(PA_{63})_7$ surface is strongly conserved upon conversion of the heptamer from prepore to pore (Fig. 7 A), despite the large motions of domain 2, in particular, which leads to formation of the Φ-clamp and membrane-spanning translocation channel (Jiang et al., 2015). Therefore, we expect the packing between LF and PA observed in our study to be preserved during the transition from prepore to pore.

Interestingly, the molecular arrangement derived from our EM reconstruction structure of a fully laden $(PA_{63})_7$–$(LF)_3$ does not preclude the presence of PA_{20} moieties attached to the counterclockwise PA_{63} (i.e., uncleaved or nicked PA_{83}; Fig. 7 B). Given the observations that PA_{20} was enriched in endocytosed complexes when the concentration of activating protease was limited (Panchal et al., 2005), it is possible that some PA_{20} remain uncleaved and bound to the protein complex in the endosomes. In that case, the PA_{20} moiety would have to unfold or dissociate in order for the translocation of its cognate LF to proceed. However, it should be noted that the N-terminal domain of PA_{83} has the greatest propensity for low pH-driven unfolding, even if uncleaved (Chalton et al., 2007). Further experiments are needed to explore the potential relevance of chimeric oligomers of PA_{63} and uncleaved PA_{83} in regulating the efficiency and order of LF translocation, as well as in promoting oligomer assembly in vivo.

The interactions between the C-terminal domain of one LF molecule and the N-terminal domain of its clockwise neighbor were completely unexpected. However, the current resolution does not allow us to define

the nature of these intermolecular interactions. Our map, calculated with 36,823 particles and film data are at a resolution of ∼15 Å. A higher-resolution EM structure would allow us to analyze the molecular determinants of the LF_C–LF_N interaction in detail. Our docking analysis and our molecular dynamics study (Alisaraie and Rouiller, 2016) suggest flexibility of the LF_C domains with a more stable LF_N–PA_{63} core. More data and higher quality data, such as that collected with a direct detector device (DDD), may also help to assess with precision inherent specimen variability.

In summary, using a combination of structural and electrophysiological data, we have provided a definitive 3-D model of a fully laden lethal toxin prepore that is consistent with the extant body of biochemical and related structural data and shown that the LF-binding rim is conserved in the membrane-bound pore. We have demonstrated the ability of the anthrax pore to translocate full-length LF in a highly efficient, fast, and robust fashion, even under the most extreme conditions. We have presented a model to rationalize this remarkable translocation efficiency, notably the unexpected presence of inter-LF interactions that may organize, stabilize, and prioritize unfolding of the critical N-terminal domains.

ACKNOWLEDGMENTS

This work was supported by the Canadian Foundation for Innovation (CFI 12824 to I. Rouiller), the Canadian Institutes for Health Research (CIHR operating grant MOP 86693 to I. Rouiller), the Natural Sciences and Engineering Research Council of Canada (NSERC DG-327201-2012 to R. Blunck and RGPIN-2014-04798 to I. Rouiller), the US Department of Defense (DoD W81XWH-10-1-0093 to R. Liddington), and the National Institutes of Health (grant CA179087 to D. Hanein and N. Volkmann). I. Rouiller and L. Fabre received a CIHR New Investigator award and fellowships from GÉPROM, respectively.

The authors declare no competing financial interests.

Merritt Maduke served as editor.

Submitted: 3 May 2016
Accepted: 25 August 2016

REFERENCES

Abrami, L., S. Liu, P. Cosson, S.H. Leppla, and F.G. van der Goot. 2003. Anthrax toxin triggers endocytosis of its receptor via a lipid raft–mediated clathrin-dependent process. *J. Cell Biol.* 160:321–328. http://dx.doi.org/10.1083/jcb.200211018

Alisaraie, L., and I. Rouiller. 2016. Molecular assembly of lethal factor enzyme and pre-pore heptameric protective antigen in early stage of translocation. *J. Mol. Model.* 22:7. http://dx.doi.org/10.1007/s00894-015-2878-8

Banks, D.J., M. Barnajian, F.J. Maldonado-Arocho, A.M. Sanchez, and K.A. Bradley. 2005. Anthrax toxin receptor 2 mediates *Bacillus anthracis* killing of macrophages following spore challenge. *Cell. Microbiol.* 7:1173–1185. http://dx.doi.org/10.1111/j.1462-5822.2005.00545.x

Basilio, D., S.J. Juris, R.J. Collier, and A. Finkelstein. 2009. Evidence for a proton-protein symport mechanism in the anthrax toxin channel. *J. Gen. Physiol.* 133:307–314. http://dx.doi.org/10.1085/jgp.200810170

Brown, M.J., K.L. Thoren, and B.A. Krantz. 2015. Role of the α clamp in the protein translocation mechanism of anthrax toxin. *J. Mol. Biol.* 427:3340–3349. http://dx.doi.org/10.1016/j.jmb.2015.08.024

Chalton, D.A., I.F. Kelly, A. McGregor, H. Ridley, A. Watkinson, J. Miller, and J.H. Lakey. 2007. Unfolding transitions of *Bacillus anthracis* protective antigen. *Arch. Biochem. Biophys.* 465:1–10. http://dx.doi.org/10.1016/j.abb.2007.04.030

Cunningham, K., D.B. Lacy, J. Mogridge, and R.J. Collier. 2002. Mapping the lethal factor and edema factor binding sites on oligomeric anthrax protective antigen. *Proc. Natl. Acad. Sci. USA.* 99:7049–7053. http://dx.doi.org/10.1073/pnas.062160399

Feld, G.K., K.L. Thoren, A.F. Kintzer, H.J. Sterling, I.I. Tang, S.G. Greenberg, E.R. Williams, and B.A. Krantz. 2010. Structural basis for the unfolding of anthrax lethal factor by protective antigen oligomers. *Nat. Struct. Mol. Biol.* 17:1383–1390. http://dx.doi.org/10.1038/nsmb.1923

Friebe, S., F.G. van der Goot, and J. Bürgi. 2016. The ins and outs of anthrax toxin. *Toxins (Basel).* 8:69. http://dx.doi.org/10.3390/toxins8030069

Gogol, E.P., N. Akkaladevi, L. Szerszen, S. Mukherjee, L. Chollet-Hinton, H. Katayama, B.L. Pentelute, R.J. Collier, and M.T. Fisher. 2013. Three dimensional structure of the anthrax toxin translocon-lethal factor complex by cryo-electron microscopy. *Protein Sci.* 22:586–594. http://dx.doi.org/10.1002/pro.2241

Groulx, N., M. Juteau, and R. Blunck. 2010. Rapid topology probing using fluorescence spectroscopy in planar lipid bilayer: the pore-forming mechanism of the toxin Cry1Aa of Bacillus thuringiensis. *J. Gen. Physiol.* 136:497–513. http://dx.doi.org/10.1085/jgp.200910347

Hohn, M., G. Tang, G. Goodyear, P.R. Baldwin, Z. Huang, P.A. Penczek, C. Yang, R.M. Glaeser, P.D. Adams, and S.J. Ludtke. 2007. SPARX, a new environment for Cryo-EM image processing. *J. Struct. Biol.* 157:47–55. http://dx.doi.org/10.1016/j.jsb.2006.07.003

Jiang, J., B.L. Pentelute, R.J. Collier, and Z.H. Zhou. 2015. Atomic structure of anthrax protective antigen pore elucidates toxin translocation. *Nature.* 521:545–549. http://dx.doi.org/10.1038/nature14247

Katayama, H., J. Wang, F. Tama, L. Chollet, E.P. Gogol, R.J. Collier, and M.T. Fisher. 2010. Three-dimensional structure of the anthrax toxin pore inserted into lipid nanodiscs and lipid vesicles. *Proc. Natl. Acad. Sci. USA.* 107:3453–3457. http://dx.doi.org/10.1073/pnas.1000100107

Kintzer, A.F., K.L. Thoren, H.J. Sterling, K.C. Dong, G.K. Feld, I.I. Tang, T.T. Zhang, E.R. Williams, J.M. Berger, and B.A. Krantz. 2009. The protective antigen component of anthrax toxin forms functional octameric complexes. *J. Mol. Biol.* 392:614–629. http://dx.doi.org/10.1016/j.jmb.2009.07.037

Klimpel, K.R., S.S. Molloy, G. Thomas, and S.H. Leppla. 1992. Anthrax toxin protective antigen is activated by a cell surface protease with the sequence specificity and catalytic properties of furin. *Proc. Natl. Acad. Sci. USA.* 89:10277–10281. http://dx.doi.org/10.1073/pnas.89.21.10277

Krantz, B.A., R.A. Melnyk, S. Zhang, S.J. Juris, D.B. Lacy, Z. Wu, A. Finkelstein, and R.J. Collier. 2005. A phenylalanine clamp catalyzes protein translocation through the anthrax toxin pore. *Science.* 309:777–781. http://dx.doi.org/10.1126/science.1113380

Lacy, D.B., M. Mourez, A. Fouassier, and R.J. Collier. 2002. Mapping the anthrax protective antigen binding site on the lethal and edema factors. *J. Biol. Chem.* 277:3006–3010. http://dx.doi.org/10.1074/jbc.M109997200

Lacy, D.B., D.J. Wigelsworth, R.A. Melnyk, S.C. Harrison, and R.J. Collier. 2004. Structure of heptameric protective antigen bound to an anthrax toxin receptor: a role for receptor in pH-dependent pore formation. *Proc. Natl. Acad. Sci. USA*. 101:13147–13151. http://dx.doi.org/10.1073/pnas.0405405101

Liu, S., Y. Zhang, M. Moayeri, J. Liu, D. Crown, R.J. Fattah, A.N. Wein, Z.X. Yu, T. Finkel, and S.H. Leppla. 2013. Key tissue targets responsible for anthrax-toxin-induced lethality. *Nature*. 501:63–68. http://dx.doi.org/10.1038/nature12510

Liu, S., M. Moayeri, and S.H. Leppla. 2014. Anthrax lethal and edema toxins in anthrax pathogenesis. *Trends Microbiol.* 22:317–325. http://dx.doi.org/10.1016/j.tim.2014.02.012

Ludtke, S.J., P.R. Baldwin, and W. Chiu. 1999. EMAN: semiautomated software for high-resolution single-particle reconstructions. *J. Struct. Biol.* 128:82–97. http://dx.doi.org/10.1006/jsbi.1999.4174

Miller, C.J., J.L. Elliott, and R.J. Collier. 1999. Anthrax protective antigen: prepore-to-pore conversion. *Biochemistry*. 38:10432–10441. http://dx.doi.org/10.1021/bi990792d

Milne, J.C., D. Furlong, P.C. Hanna, J.S. Wall, and R.J. Collier. 1994. Anthrax protective antigen forms oligomers during intoxication of mammalian cells. *J. Biol. Chem.* 269:20607–20612.

Milne, J.C., S.R. Blanke, P.C. Hanna, and R.J. Collier. 1995. Protective antigen-binding domain of anthrax lethal factor mediates translocation of a heterologous protein fused to its amino- or carboxy-terminus. *Mol. Microbiol.* 15:661–666. http://dx.doi.org/10.1111/j.1365-2958.1995.tb02375.x

Mindell, J.A., and N. Grigorieff. 2003. Accurate determination of local defocus and specimen tilt in electron microscopy. *J. Struct. Biol.* 142:334–347. http://dx.doi.org/10.1016/S1047-8477(03)00069-8

Mogridge, J., K. Cunningham, and R.J. Collier. 2002. Stoichiometry of anthrax toxin complexes. *Biochemistry*. 41:1079–1082. http://dx.doi.org/10.1021/bi015860m

Panchal, R.G., K.M. Halverson, W. Ribot, D. Lane, T. Kenny, T.G. Abshire, J.W. Ezzell, T.A. Hoover, B. Powell, S. Little, et al. 2005. Purified *Bacillus anthracis* lethal toxin complex formed in vitro and during infection exhibits functional and biological activity. *J. Biol. Chem.* 280:10834–10839. http://dx.doi.org/10.1074/jbc.M412210200

Pannifer, A.D., T.Y. Wong, R. Schwarzenbacher, M. Renatus, C. Petosa, J. Bienkowska, D.B. Lacy, R.J. Collier, S. Park, S.H. Leppla, et al. 2001. Crystal structure of the anthrax lethal factor. *Nature*. 414:229–233. http://dx.doi.org/10.1038/n35101998

Park, S., and S.H. Leppla. 2000. Optimized production and purification of *Bacillus anthracis* lethal factor. *Protein Expr. Purif.* 18:293–302. http://dx.doi.org/10.1006/prep.2000.1208

Petosa, C., R.J. Collier, K.R. Klimpel, S.H. Leppla, and R.C. Liddington. 1997. Crystal structure of the anthrax toxin protective antigen. *Nature*. 385:833–838. http://dx.doi.org/10.1038/385833a0

Pimental, R.-A.L., K.A. Christensen, B.A. Krantz, and R.J. Collier. 2004. Anthrax toxin complexes: heptameric protective antigen can bind lethal factor and edema factor simultaneously. *Biochem. Biophys. Res. Commun.* 322:258–262. http://dx.doi.org/10.1016/j.bbrc.2004.07.105

Plotkin, S.A., P.S. Brachman, M. Utell, F.H. Bumford, and M.M. Atchison. 2002. An epidemic of inhalation anthrax, the first in the twentieth century: I. Clinical features. 1960. *Am. J. Med.* 112:4–12. http://dx.doi.org/10.1016/S0002-9343(01)01050-6

Ren, G., J. Quispe, S.H. Leppla, and A.K. Mitra. 2004. Large-scale structural changes accompany binding of lethal factor to anthrax protective antigen: a cryo-electron microscopic study. *Structure*. 12:2059–2066. http://dx.doi.org/10.1016/j.str.2004.09.010

Santelli, E., L.A. Bankston, S.H. Leppla, and R.C. Liddington. 2004. Crystal structure of a complex between anthrax toxin and its host cell receptor. *Nature*. 430:905–908. http://dx.doi.org/10.1038/nature02763

Scheres, S.H., R. Núñez-Ramírez, C.O. Sorzano, J.M. Carazo, and R. Marabini. 2008. Image processing for electron microscopy single-particle analysis using XMIPP. *Nat. Protoc.* 3:977–990. http://dx.doi.org/10.1038/nprot.2008.62

Slater, L.H., E.C. Hett, A.E. Clatworthy, K.G. Mark, and D.T. Hung. 2013. CCT chaperonin complex is required for efficient delivery of anthrax toxin into the cytosol of host cells. *Proc. Natl. Acad. Sci. USA*. 110:9932–9937. http://dx.doi.org/10.1073/pnas.1302257110

Tama, F., G. Ren, C.L. Brooks III, and A.K. Mitra. 2006. Model of the toxic complex of anthrax: responsive conformational changes in both the lethal factor and the protective antigen heptamer. *Protein Sci.* 15:2190–2200. http://dx.doi.org/10.1110/ps.062293906

Tamayo, A.G., L. Slater, J. Taylor-Parker, A. Bharti, R. Harrison, D.T. Hung, and J.R. Murphy. 2011. GRP78(BiP) facilitates the cytosolic delivery of anthrax lethal factor (LF) in vivo and functions as an unfoldase in vitro. *Mol. Microbiol.* 81:1390–1401. http://dx.doi.org/10.1111/j.1365-2958.2011.07770.x

Thoren, K.L., E.J. Worden, J.M. Yassif, and B.A. Krantz. 2009. Lethal factor unfolding is the most force-dependent step of anthrax toxin translocation. *Proc. Natl. Acad. Sci. USA*. 106:21555–21560. http://dx.doi.org/10.1073/pnas.0905880106

Volkmann, N. 2002. A novel three-dimensional variant of the watershed transform for segmentation of electron density maps. *J. Struct. Biol.* 138:123–129. http://dx.doi.org/10.1016/S1047-8477(02)00009-6

Volkmann, N. 2009. Confidence intervals for fitting of atomic models into low-resolution densities. *Acta Crystallogr. D Biol. Crystallogr.* 65:679–689. http://dx.doi.org/10.1107/S0907444909012876

Volkmann, N. 2014. The joys and perils of flexible fitting. *Adv. Exp. Med. Biol.* 805:137–155. http://dx.doi.org/10.1007/978-3-319-02970-2_6

Volkmann, N., and D. Hanein. 1999. Quantitative fitting of atomic models into observed densities derived by electron microscopy. *J. Struct. Biol.* 125:176–184. http://dx.doi.org/10.1006/jsbi.1998.4074

Volkmann, N., and D. Hanein. 2003. Docking of atomic models into reconstructions from electron microscopy. *Methods Enzymol.* 374:204–225. http://dx.doi.org/10.1016/S0076-6879(03)74010-5

Weiner, Z.P., and I.J. Glomski. 2012. Updating perspectives on the initiation of *Bacillus anthracis* growth and dissemination through its host. *Infect. Immun.* 80:1626–1633. http://dx.doi.org/10.1128/IAI.06061-11

Wynia-Smith, S.L., M.J. Brown, G. Chirichella, G. Kemalyan, and B.A. Krantz. 2012. Electrostatic ratchet in the protective antigen channel promotes anthrax toxin translocation. *J. Biol. Chem.* 287:43753–43764. http://dx.doi.org/10.1074/jbc.M112.419598

Xu, X.P., I. Rouiller, B.D. Slaughter, C. Egile, E. Kim, J.R. Unruh, X. Fan, T.D. Pollard, R. Li, D. Hanein, and N. Volkmann. 2012. Three-dimensional reconstructions of Arp2/3 complex with bound nucleation promoting factors. *EMBO J.* 31:236–247. http://dx.doi.org/10.1038/emboj.2011.343

Zhang, S., K. Cunningham, and R.J. Collier. 2004. Anthrax protective antigen: efficiency of translocation is independent of the number of ligands bound to the prepore. *Biochemistry*. 43:6339–6343. http://dx.doi.org/10.1021/bi049794a

Zheng, S., G. Zhang, J. Li, and P.R. Chen. 2014. Monitoring endocytic trafficking of anthrax lethal factor by precise and quantitative protein labeling. *Angew. Chem. Int. Ed. Engl.* 53:6449–6453. http://dx.doi.org/10.1002/anie.201403945